

Measuring Mass Transfer of *n*-Hexane and 2-Chloroethyl Ethyl Sulfide in Sorbent/Polymer Fiber Composites Using a Volumetric Adsorption Apparatus

Florencia A. Son, Kaihang Shi,* Randall Q. Snurr,* and Omar K. Farha*



Cite This: <https://doi.org/10.1021/acsami.4c02117>



Read Online

ACCESS |

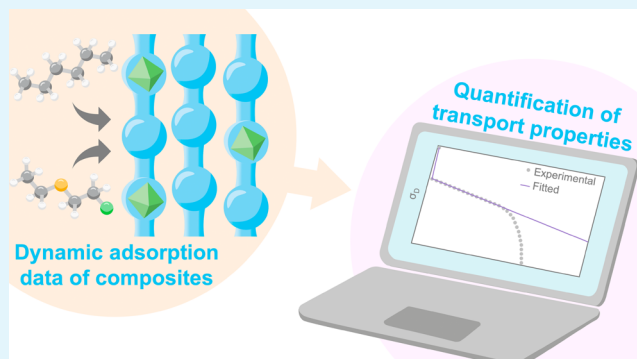
Metrics & More

Article Recommendations

Supporting Information

ABSTRACT: The integration of metal–organic frameworks (MOFs) into composite systems serves as an effective strategy to increase the processability of these materials. Notably, MOF/fiber composites have shown much promise as protective equipment for the capture and remediation of chemical warfare agents. However, the practical application of these composites requires an understanding of their mass transport properties, as both mass transfer resistance at the surface and diffusion within the materials can impact the efficacy of these materials. In this work, we synthesized composite fibers of MOF-808 and amidoxime-functionalized polymers of intrinsic microporosity (PIM-1-AX) and measured the adsorption and mass transport behavior of *n*-hexane and 2-chloroethyl ethyl sulfide (CEES), a sulfur mustard simulant. We developed a new Fickian diffusion model for cylindrical shapes to fit the dynamic adsorption data obtained from a commercial volumetric adsorption apparatus and found that mass transport behavior in composite fibers closely resembled that in the pure PIM fibers, regardless of MOF loading. Moreover, we found that *n*-hexane adsorption mirrors that of CEES, indicating that it could be used as a structural mimic for future adsorption studies of the sulfur mustard simulant. These preliminary insights and the new model introduced in this work lay the groundwork for the design of next-generation composite materials for practical applications.

KEYWORDS: metal–organic frameworks, fibers, composites, mass transport, surface permeation



INTRODUCTION

Metal–organic frameworks (MOFs) are porous, crystalline materials¹ that are promising adsorbents and/or catalysts for a multitude of applications.^{2–6} However, their practical application can be hindered by the fact that these nanoporous MOFs are often synthesized in a powder form with nanometer or micron sized particles. Therefore, the implementation of MOFs for relevant applications requires additional processing techniques. Shape and form engineering methods, such as pelletization, extrusion, or granulation,^{7–11} are effective strategies for the integration of MOF crystallites in industrial applications. Beyond these approaches, interest has grown in the incorporation of MOFs onto support materials to generate a composite material that enables their use in practical applications.

Substrates that have previously been explored include membranes,¹² ceramics,¹³ foams,¹⁴ and fibers.^{15–24} Of note are MOF-based composites fabricated with fibers^{15,25} that provide the final material with processability, which is advantageous for the development of personal protective equipment against chemical warfare agents.^{19,20,26–30} MOF/fiber composites can be fabricated using methods including a MOF-first strategy, a MOF attachment strategy, and a fiber-

first strategy.²⁵ Due to the varying properties that may arise based on the assembly of the MOF and fibers, it is critical to develop structure–property relationships, particularly relating to diffusion, within these systems.

Studying mass transport in porous materials is necessary for their application as both catalysts and adsorbents.^{31–33} However, delineating the relative contributions to mass transport from diffusion within the bulk material versus surface permeation remains challenging.^{34,35} Care must be taken to apply the most accurate models when fitting experimental data. For instance, transport in fibrous materials can be considered along their axial³⁶ or radial directions,^{37,38} ultimately dependent on the fiber structure and aspect ratio.³⁹ In addition, experimental characterization of molecular transport typically requires specialized and expensive facilities, such as confocal

Received: February 5, 2024

Revised: May 19, 2024

Accepted: May 19, 2024

Raman microscopy⁴⁰ or infrared Raman microscopy;⁴¹ although these methods provide beneficial insights, they suffer from limited accessibility, inhibiting the development of new applications of porous materials.

Herein, we synthesized MOF/fiber composites using MOF-808, a borderline micro/mesoporous Zr(IV)-based MOF with 6-connected nodes and tritopic linkers,⁴² which we obtained using an aqueous synthesis,⁴³ and an amidoxime-functionalized polymer of intrinsic microporosity (PIM) known as PIM-1-AX.^{44–46} PIMs are inherently microporous owing to their highly rigid and contorted molecular structures that cannot fill space efficiently.^{47–49} These hydrophobic polymers have been demonstrated to be effective for toxic gas capture⁵⁰ and to be breathable but not permeable to liquid water, which are desirable qualities for protective gear.⁵¹ We previously demonstrated that porous fibrous mats of the amidoxime-functionalized PIM and a polyoxometalate were effective for the oxidative degradation of 2-chloroethyl ethyl sulfide (CEES), a sulfur mustard simulant.⁴⁶ As such, in our study of reactive fibers, we elected to utilize PIM-1-AX for this work. Through an electrospinning process, we successfully encapsulated varying loadings of MOF-808 particles within PIM-1-AX (Figure 1). We also developed a new Fickian diffusion model

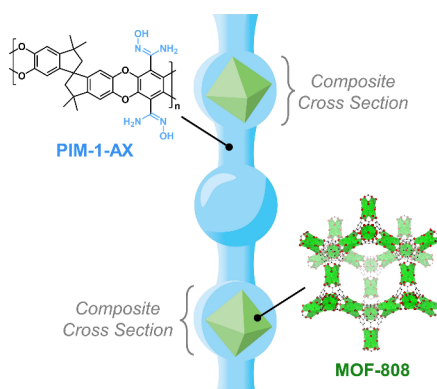
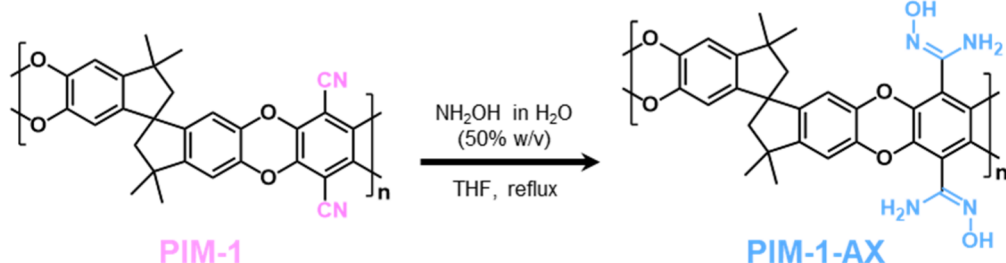


Figure 1. Depiction of MOF/PIM-1-AX composite fiber, where PIM-1-AX encapsulates MOF-808 particles.

to quantitatively characterize the surface permeation and in-pore diffusion of molecules in MOF/fiber composites having cylindrical shapes. The new diffusion model takes input data from a commercial volumetric adsorption instrument,^{52,53} which is readily accessible in many laboratories compared to other specialized facilities for studying molecular diffusion. Finally, we looked at the adsorption and mass transport of *n*-hexane and CEES in these composite materials.

Scheme 1. Reaction of PIM-1 to PIM-1-AX



EXPERIMENTAL METHODS

PIM-1-AX Synthesis. We first synthesized PIM-1 through the aromatic nucleophilic substitution reaction between 3,3,3',3'-tetramethyl-1,1''-spirobisindane-5,5',6,6'-tetrol and 2,3,5,6-tetrafluorophthalonitrile.^{45,47,50} To introduce the amidoxime moiety, the nitrile groups of PIM-1 were reacted with hydroxylamine, yielding PIM-1-AX (Scheme 1).^{44,45,50} Both PIMs were characterized using ¹H nuclear magnetic resonance (NMR) spectroscopy (Figure S1) and diffuse reflectance infrared Fourier transform spectroscopy (DRIFTS) (Figure S2). Complete conversion from PIM-1 to PIM-1-AX was confirmed by comparing the DRIFTS spectra, which showed the loss of the nitrile peak occurring at 2239 cm⁻¹ (Figure S2).⁴⁴

Electrospinning Fibers. MOF-808 and PIM-1-AX fiber composites were synthesized via an electrospinning process,^{46,50,51,54} a technique that uses electrostatic forces to produce fibers from polymer solutions. Conditions (polymer concentration, solvent, flow rate, voltage, and distance between tip and collector) were optimized to obtain bead-free and uniform fibers. Further information can be found in the Supporting Information.

Fickian Diffusion Model for Materials having Cylindrical Shapes. Brandani and co-workers developed Fickian transport models that are compatible with widely available volumetric measurement systems. The theoretical framework allows them to consider the effects of diffusion⁵³ and surface resistance⁵⁵ separately or in a combined manner.⁵⁶ In this work, we performed transient uptake measurements on a Micromeritics 3Flex Surface Characterization Analyzer, which has an accuracy limit of 10⁻⁶ Torr. When rendering the instrument to its most basic components, it consists of a dosing cell and an uptake (or sample) cell that are separated by a valve (Figure 2). Transient pressure data were collected during the

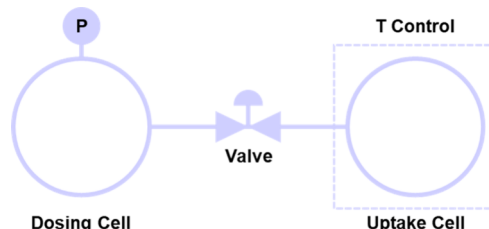


Figure 2. Depiction of a volumetric adsorption system.

entire duration of the isotherm measurements; each new dose of the probe introduced to the uptake cell was fitted to the Fickian transport model. To minimize error in our mass transport measurements, low pressure regions prior to the saturation of the porous materials were analyzed so that the changes in pressure could most accurately be measured by the instrument.⁵² Mass transfer in MOF-808 was fitted according to our previously published protocol, which uses the assumption of spherical particles.^{52,53,56} However, due to the high aspect ratio of the fibers, arising from the continuous generation of the fibers via the electrospinning process, a new diffusion model is needed to capture transport in an infinitely long cylindrical shape where mass transport occurs in a radial direction.^{37,38}

Here we adopted the framework of Brandani et al. and extended the theory to materials of cylindrical shapes. By assuming the ideal gas condition in the system when the pressure is sufficiently low, the mass balance of the volumetric adsorption system (Figure 2) in each dosing cycle is described by the following equations:

$$\frac{dn}{dt} = -\frac{V_d}{\mathcal{R}T_d} \frac{dP_d}{dt} \quad (1)$$

$$\frac{dn}{dt} = \bar{\chi}(P_d - P_u) \quad (2)$$

$$\frac{dn}{dt} = \epsilon V_u \frac{dc}{dt} + V_s \frac{d\bar{q}}{dt} \quad (3)$$

Equation 1 assumes ideal gas behavior and relates the rate of mass change (dn/dt) in the uptake cell to the rate of pressure change (dP_d/dt) in the dosing cell (subscript d) at temperature T_d , where V_d and \mathcal{R} are the volume of the dosing cell and gas constant, respectively. **Equation 2** accounts for the effect of the valve resistance on the mass flow from the dosing cell to the uptake cell, where $\bar{\chi}$ is the valve constant that is intrinsic to the instrument, and P_u is the pressure in the uptake cell (subscript u). **Equation 3** establishes the mass balance

in the uptake cell, i.e., the total rate of mass change (dn/dt) is equal to the summation of the mass change in the (free) volume of the uptake cell (the first term on the right) and the mass change in the adsorbed phase (the second term on the right). Here we assume that the volume of the solid adsorbent, V_s , is negligible compared to the volume of the uptake cell, V_u ; thus the void fraction of the uptake cell, ϵ , is simply 1. The rate of change of spatially averaged adsorbed concentration, $d\bar{q}/dt$, can be derived from spatially averaging of Fick's second law in a cylindrical geometry over the entire cylindrical material.

By solving **eqs 1–3** together with Fick's second law in a cylindrical geometry⁵⁷ in the Laplace domain (full derivation is available in the **Supporting Information**), we can obtain an expression for the dimensionless pressure in the dosing cell, $\rho_d = (P_d - P_u^0)/(P_\infty - P_u^0)$, where P_u^0 and P_∞ are initial pressure ($t = 0$, superscript 0) in the uptake cell and the equilibrium pressure ($t = \infty$, subscript ∞), respectively. The expression is given by

$$\frac{\rho_d}{\rho_d^0} = \frac{2\delta}{1 + 2\gamma + 2\delta} + \sum_{i=1}^M a_i \exp\left(-\beta_i^2 \frac{D}{R^2} t\right) \quad (4)$$

where $M = 100$ was used in our calculations, and

$$a_i = \frac{z_i - \gamma\beta_i^2 + \omega\delta}{\omega\delta + z_i - \gamma\beta_i^2 + (\omega - \beta_i^2)\left(\gamma - \frac{z_i}{2\beta_i}\left(\frac{1}{\beta_i} + \frac{J_0 - J_2}{2J_1}\right) + \frac{z_i^2}{2\beta_i}\left(\frac{1}{\beta_i} + \frac{1}{\alpha\beta_i} + \frac{J_0 - J_2}{2\alpha J_1}\right)\right)} \quad (5)$$

$$z_i = \frac{\omega\delta\beta_i^2}{\omega - \beta_i^2} + \gamma\rho_i^0 \quad (6)$$

and β_i are the positive (nonzero) roots of the following transcendental equation:

$$\frac{\alpha\beta_j}{\alpha J_0 - \beta_j J_1} + z_i = 0 \quad (7)$$

In **eqs 5** and **7**, the Bessel functions of the first kind $J_n(\beta_i)$ ($n = 0, 1, 2$) are written as shorthand J_n for convenience. ρ_d^0 is the initial dimensionless pressure in the dosing cell in a certain dosing cycle, and R is the radius of the cylindrical fiber (composites). The in-pore transport diffusivity is D , and $\alpha = kR/D$ where k is the surface permeability of the adsorbent. δ , γ , and ω are dimensionless parameters that contain information about the volumetric system and the adsorption process (see the **Supporting Information**), with $\omega \propto \bar{\chi}/D$.

Since the equilibrium pressures P_∞ and initial pressures P_d^0 and P_u^0 are known from experiments, we can obtain a relation for δ and γ from **eq 4**, as the second term on the right-hand side of the equation simply vanishes at $t = \infty$:

$$\frac{(P_\infty - P_u^0)}{(P_d^0 - P_u^0)} = \frac{2\delta}{1 + 2\gamma + 2\delta} \quad (8)$$

We also note that according to the definitions of δ and γ (see the **Supporting Information** for details), we can obtain the additional relation:

$$\frac{\delta}{\gamma} = \frac{V_d T_u}{\epsilon V_u T_d} \quad (9)$$

where V_d , V_u , T_d , and T_u are known constants that are intrinsic to the experimental setup. The void fraction ϵ is assumed to be 1. Then using **eqs 8** and **9**, we can solve for both δ and γ .

As mentioned by Brandani,⁵³ the valve constant, $\bar{\chi}$, determines the initial pressure response. We found that the rate of initial pressure

drops in ρ_d in our data varies across different pressure doses. Thus, unlike Son et al.⁵² where $\bar{\chi}$ was preserved as a constant for all pressure doses fits, here we treated $\bar{\chi}$ as a fitting parameter for each pressure dose. This leaves D , α , and ω as unknown parameters, which were fitted by minimizing the root-mean-square error (RMSE) between the model predictions using **eqs 4–7** and the experimental reduced pressure drop, σ_D , in the dosing cell, defined as⁵⁵

$$\sigma_D = \frac{P_d - P_\infty}{P_d^0 - P_\infty} = \frac{\rho_d(P_\infty - P_u^0) + P_u^0 - P_\infty}{P_d^0 - P_\infty} \quad (10)$$

Multiple initial guesses were attempted for fitting parameters D , α , and ω , and the final fitting was chosen to have the lowest RMSE among all trial fittings, yielding the transport diffusivity D and the surface permeability k as the primary outputs of the model. **Figure 3** shows a representative fitting to the experimental transient adsorption data using the new cylindrical model. We have implemented our model in a Python Jupyter notebook. The code and an example

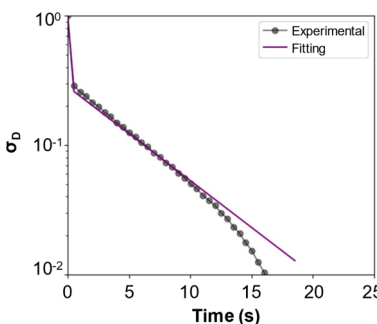


Figure 3. Representative fitting of the new cylindrical transport model (purple line) to the experimental transient adsorption data (black points connected with line), in a semilog plot of reduced pressure drop σ_D versus time for *n*-hexane adsorption in 10% w/w MOF-808/PIM-1-AX fibers at 298 K and pressure dose around 3.7 Torr. The experimental data file for this system is available in the **Supporting Information** and is ready to use with the provided Python code for model fitting.

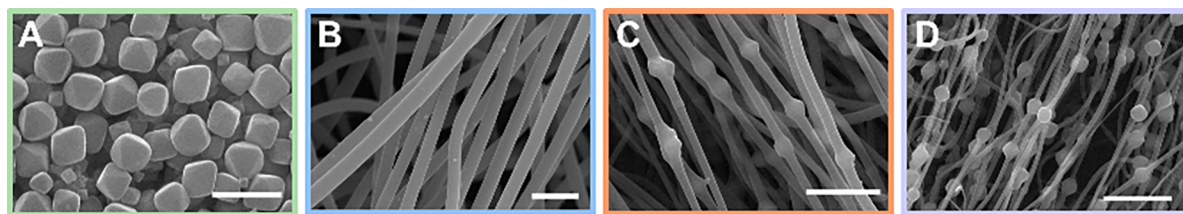


Figure 4. SEM images of A) MOF-808, B) PIM-1-AX fibers, C) 10% w/w MOF-808/PIM-1-AX fibers, and D) 30% w/w MOF-808/PIM-1-AX fibers. Scale bars represent 2 μm for A and 5 μm for B–D.

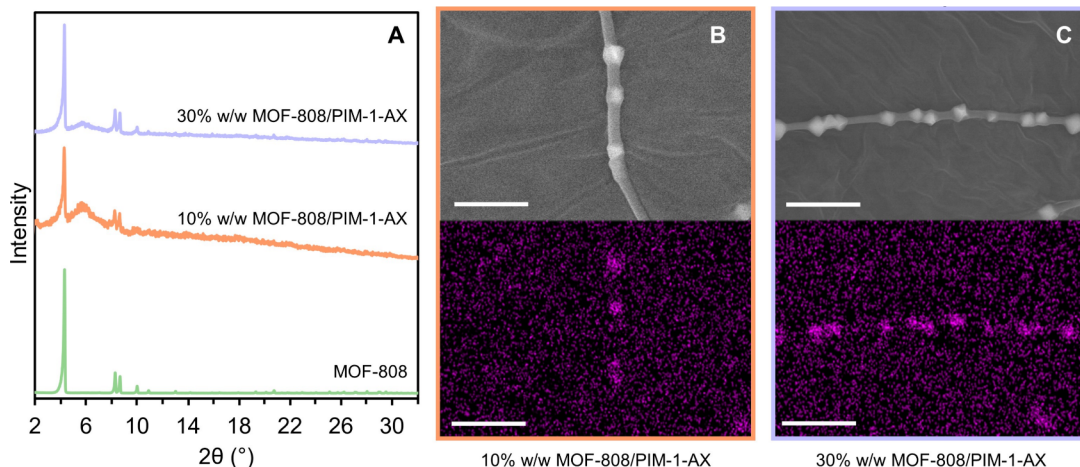


Figure 5. Characterization of MOF-808/PIM-1-AX composites. A) PXRD patterns. B) Back scattering electron image (top) and EDS map of Zr $\text{L}\alpha 1$ (bottom) of 10% w/w MOF-808/PIM-1-AX fiber. C) Back scattering electron image (top) and EDS map of Zr $\text{L}\alpha 1$ (bottom) of 30% w/w MOF-808/PIM-1-AX fiber. Scale bars represent 5 μm .

Table 1. Textural Properties of MOF, Polymer, and Composite Materials

sample	BET area (m^2/g)	dominant pore size(s) (\AA)	pore volume(cm^3/g)	MOF-808 (% w/w)	R (μm)
MOF-808	2100	17	0.83	100	0.55 ± 0.10
PIM-1-AX	415	7, 13, 26	0.21	0	1.15 ± 0.25
10% w/w MOF-808/PIM-1-AX	615	7, 13, 17	0.31	10.4 ± 0.1	0.40 ± 0.15
30% w/w MOF-808/PIM-1-AX	1000	7, 16	0.43	34.0 ± 0.4	0.35 ± 0.20

experimental data input file (data in Figure 3) are available in the Supporting Information.

RESULTS AND DISCUSSION

We first verified the successful incorporation of $\sim 1 \mu\text{m}$ MOF particles into polymeric fibers using scanning electron microscopy (SEM). SEM images revealed an average particle size of $1.1 \pm 0.2 \mu\text{m}$ for MOF-808 (Figure 4A) and average fiber widths of $2.3 \pm 0.5 \mu\text{m}$ for PIM-1-AX (Figure 4B), $0.8 \pm 0.3 \mu\text{m}$ for 10% w/w MOF-808/PIM-1-AX (Figure 4C), and $0.7 \pm 0.4 \mu\text{m}$ for 30% w/w MOF-808/PIM-1-AX (Figure 4D). As the fiber widths for the composites were not uniform, owing to the differences between the regions with pure PIM-1-AX compared to MOF-808/PIM-1-AX, we estimated the fiber radial dimension to be an average of the two. SEM images additionally confirmed that the fiber samples were uniform and bead-free.

To corroborate the incorporation and encapsulation of MOF-808 inside the polymer fibers, we used powder X-ray diffraction (PXRD) as well as energy-dispersive X-ray spectroscopy (EDS). The characteristic MOF-808 peaks remained intact in the PXRD patterns of the MOF-808/PIM-1-AX composites (Figure 5A). Moreover, backscattering electron images and EDS maps confirmed the encapsulation of the

MOF-808 particles by PIM-1-AX (Figures 5B,C), rather than MOF attachment on the exterior of the fibers. Finally, to quantify the amount of Zr in the fibers, we obtained inductively coupled plasma-optical emission spectroscopy (ICP-OES) results, which confirmed loadings of 10.4 ± 0.1 wt % and 34.0 ± 0.4 wt % MOF-808 in the composites (Table 1). As such, measurements conducted with our composite materials will be denoted as 10% w/w MOF-808/PIM-1-AX and 30% w/w MOF-808/PIM-1-AX. Notably, the final MOF-808 loadings were consistent with the initial quantities used with their respective electrospinning solutions and were comparable among various areas of the fibers, which alludes to the fairly uniform dispersion of the MOF particles.

Finally, we measured nitrogen sorption isotherms of the materials at 77 K (Figure 6) to probe their textural properties. As anticipated, the pore volumes and BET areas increased with increasing MOF-808 incorporation, due to the higher porosity of the MOF compared to the PIM-1-AX. BET areas were calculated to be $2100 \text{ m}^2/\text{g}$ for MOF-808, $415 \text{ m}^2/\text{g}$ for PIM-1-AX, $615 \text{ m}^2/\text{g}$ for 10% w/w MOF-808/PIM-1-AX, and $1000 \text{ m}^2/\text{g}$ for 30% w/w MOF-808/PIM-1-AX. The ~ 7 and $\sim 17 \text{ \AA}$ pores of PIM-1-AX and MOF-808, respectively, were maintained in the composite systems (Figure S3). Moreover, using the assumption that the porosity of the pure PIM

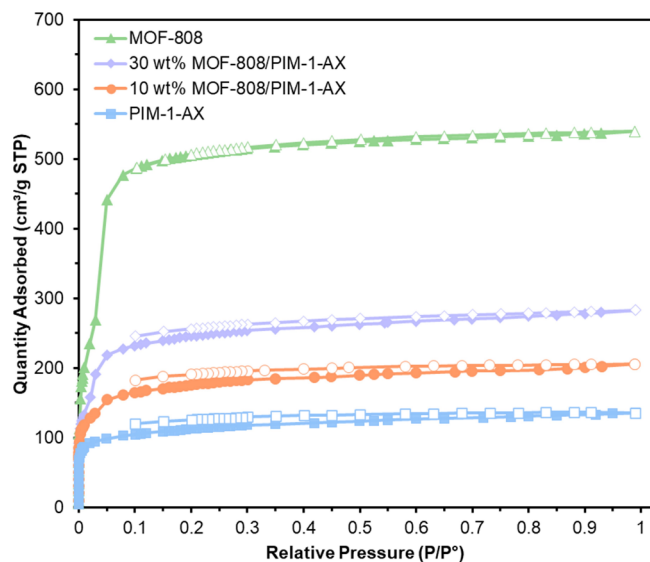


Figure 6. Nitrogen adsorption (closed markers) and desorption (open markers) isotherms at 77 K of MOF-808, PIM-1-AX, and two composite materials.

polymer was maintained, the BET areas of MOF-808 were calculated to be $2340 \text{ m}^2/\text{g}$ for the 10% w/w MOF-808/PIM-1-AX fiber and $2135 \text{ m}^2/\text{g}$ for the 30% w/w MOF-808/PIM-1-AX fibers, indicating that MOF accessibility was maintained. We used the successfully synthesized composite fibers for the sorption measurements (Figures S4 and S5) and mass transport quantification (Figures S6–S11) for this study.

We began our adsorption and transport studies by using *n*-hexane as a structural mimic for CEES (Figure 7). The loading of *n*-hexane at saturation was consistent with N_2 sorption

measurements, where higher porosity materials resulted in higher *n*-hexane uptake (Figure 7A). At lower pressure regions, the samples with PIM-1-AX had higher affinity for *n*-hexane, owing to the organophilic nature of the PIM (Figure 7B). When looking at the surface permeabilities of the samples (Figure 7C), no clear differences were apparent for the composite materials and the pure MOF. However, when looking at the intrinsic surface permeability k/R (Figure 7D), which removes the particle size dependence for easier comparison across different samples, we can begin to see a moderate trend of decreasing k/R with increasing MOF loadings. Intrinsic surface permeability is proportional to $1/\tau_{bar}$, where τ_{bar} is the mean lifetime if the transport process is exclusively controlled by the surface barrier.^{58,59} The pure PIM-1-AX fibers had the largest intrinsic surface permeabilities, whereas the pure MOF-808 particles had the lowest. MOF-808 and 30% w/w MOF-808/PIM-1-AX have intrinsic surface permeabilities around 0.01 s^{-1} , which have previously been attributed to surface defects.^{60–62} In contrast, while the PIM-1-AX and 10% w/w MOF-808/PIM-1-AX fibers commenced at 0.01 s^{-1} , the surface barriers decreased with higher pressures with intrinsic surface permeabilities increasing approximately 6- and 3-fold, respectively, at 2 Torr. As all materials are microporous, with MOF-808 containing pore apertures of 14 \AA that lead into the $\sim 17 \text{ \AA}$ cavities, we hypothesize that MOF-808 deviates from its ideal structure and has surface defects, e.g., permanently collapsed and blocked channel termini upon materials activation, present that induce the observed surface barriers. This may explain the independence of the surface permeability on external pressure for MOF-808 (Figure 7C,D).⁶² The correlation between pressure and surface permeability increases as the concentration of MOF-808 in fiber samples decreases. While future work is required to better understand this phenomenon, we posit that the increase of

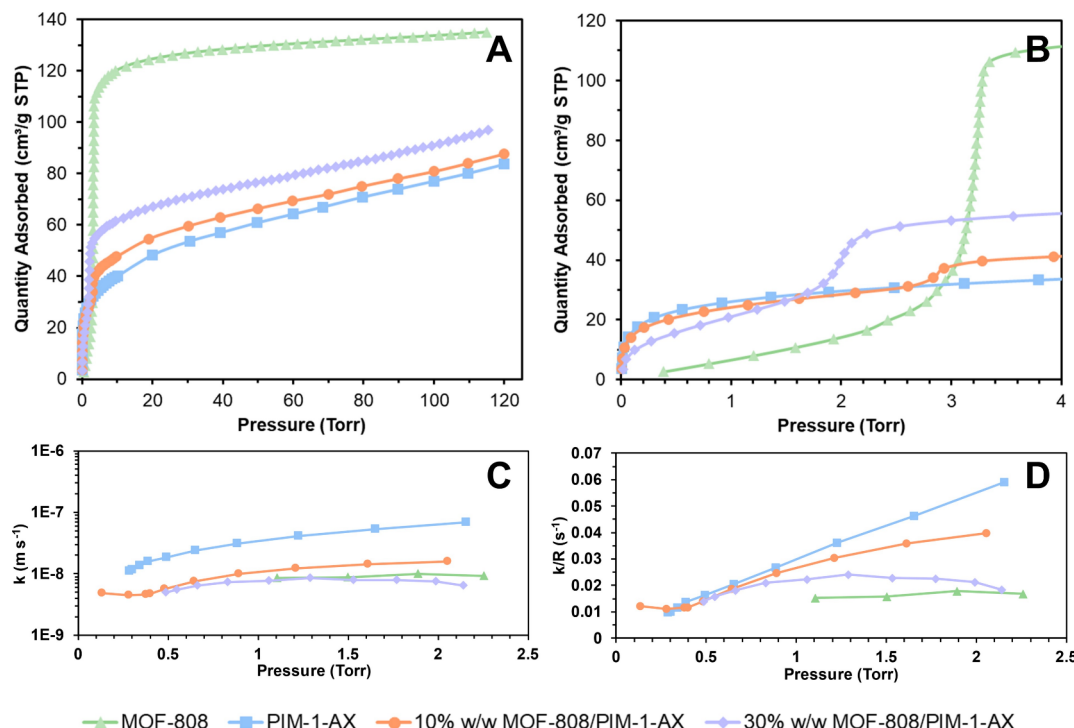


Figure 7. *n*-Hexane isotherms at 298 K of MOF-808, PIM-1-AX fibers, and MOF-808/PIM-1-AX fiber composites. A) Full isotherms. B) Low pressure region. C) Surface permeabilities. D) Intrinsic surface permeabilities.

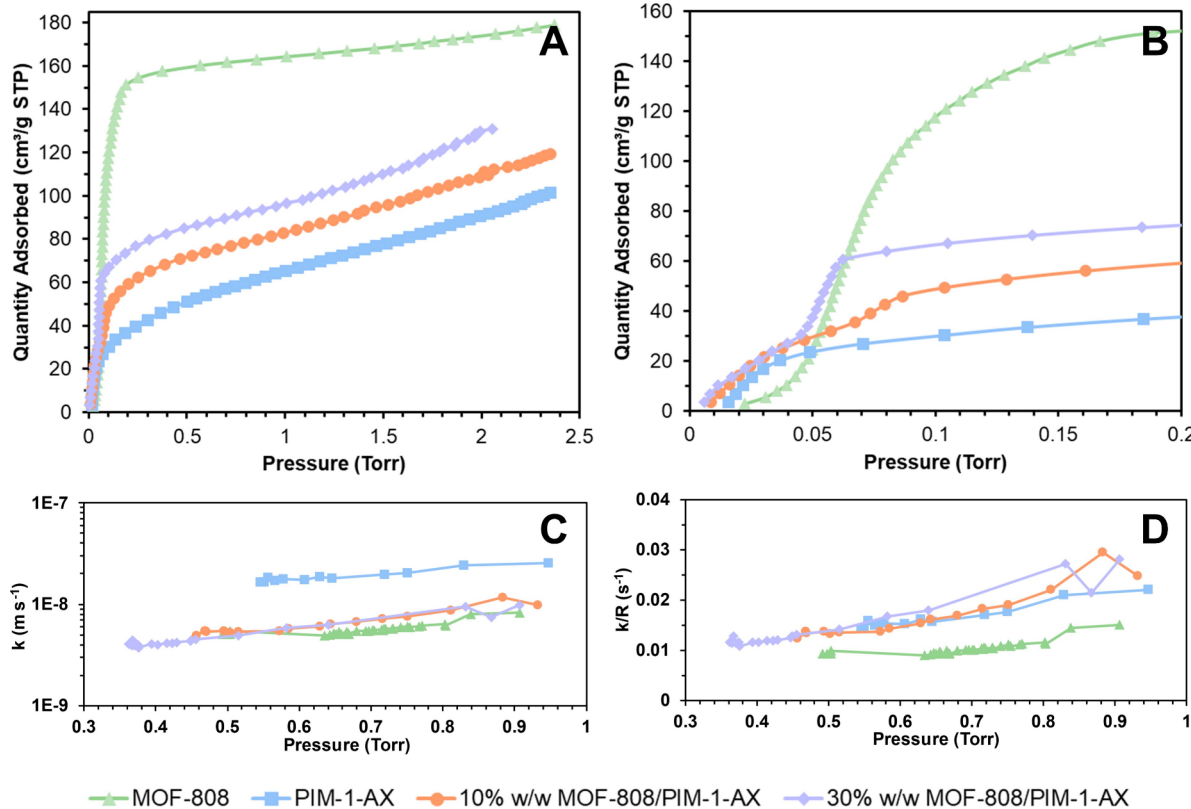


Figure 8. CEES isotherms at 298 K of MOF-808, PIM-1-AX fibers, and MOF-808/PIM-1-AX fiber composites. A) Full isotherms. B) Low pressure region. C) Surface permeabilities. D) Intrinsic surface permeabilities.

external pressure facilitates the entrance of molecules into PIM micropores. The higher *n*-hexane density at the PIM fiber surface can possibly facilitate diffusion through the partially occluded channel termini,⁶² while such effects are smeared by the increased loading of MOFs that contain permanently collapsed channel termini at or near the surface. We note, however, that these observed differences are minor as the intrinsic surface permeabilities are within the same order of magnitude.

Similar to our previous mass transport studies,^{52,62} the fitted dimensionless parameter, $\alpha = kR/D$, in this study was less than 1 and lower than 0.1 in most experimental trials. This indicates that the transport process into the porous material was dominated by the surface barriers.⁵⁸ In practice, we found that starting from different initial guesses, a good model fitting might end up with drastically different D values (differing by 1 order of magnitude for example), while the fitted surface permeability, k , is almost identical across different runs. As such, we were only able to reliably determine the surface permeability and unable to accurately quantify the in-pore transport diffusivity, D , in our fiber samples.

The adsorption isotherms of CEES (Figure 8A,B) in our samples were similar to those of *n*-hexane, indicating that *n*-hexane can serve as a reasonable structural mimic of CEES to study adsorption behavior. When considering mass transfer, the intrinsic surface permeabilities of CEES in all fiber samples compared to those of *n*-hexane had more negligible differences (Figure 8D). All fiber samples had slightly higher intrinsic surface permeabilities of around 0.015 s^{-1} compared to 0.01 s^{-1} for the MOF-808 particles (Figure 8D). As the variability of intrinsic surface permeability among fiber samples was minor, however, there were no trends evident, deviating from

the *n*-hexane results and indicating that *n*-hexane would not serve as an accurate simulant for mass transport studies within similar project scopes to ours. We hypothesize that across our different fiber samples, surface permeation is not favorable due to the stronger adsorbate–adsorbent interactions, e.g., halogen bonding, present when using CEES as a probe. The interactions present may result in strong adsorption onto the surface of the fibers, slowing down the movement of the probe molecules into the pores. Notably, while experimental efforts have been made to understand equilibrium adsorption of CWAs and their simulants in MOFs,^{63,64} diffusion studies have predominantly been limited to computational efforts.^{65–67} Therefore, this work will provide the community with preliminary insights into the diffusivity of a CWA simulant in both MOFs and MOF/fiber composites.

CONCLUSIONS

Through an electrospinning process, we successfully encapsulated 10% w/w and 30% w/w MOF-808 particles within PIM-1-AX. Using a newly developed cylindrical Fickian diffusion model, we quantified mass transport properties of both *n*-hexane and CEES, a sulfur mustard simulant in these materials. We found that transport is dominated by surface barriers, and diffusion within the bulk of the composite materials is fast in comparison. While there were minor differences in the mass transport properties of the composite fiber materials, overall, the intrinsic surface permeabilities were comparable across different types of PIM/MOF composites and pure PIM fibers, indicating that MOF/fiber composites can be implemented without negative ramifications on mass transfer. Additionally, our results demonstrate that as adsorption behavior is similar for *n*-hexane and CEES, the former could be used in future

sorption studies as a more accessible structural mimic. We hope that these preliminary results will not only serve as a guide to the community for the rational design of MOF composite systems but that the developed cylindrical diffusion model will also encourage others to explore mass transport in composite fibers.

■ ASSOCIATED CONTENT

SI Supporting Information

The Supporting Information is available free of charge at <https://pubs.acs.org/doi/10.1021/acsami.4c02117>.

Python Jupyter notebook for performing the transport model fitting and an example experimental data input file ([ZIP](#))

Experimental procedures, powder X-ray diffraction patterns, N₂ isotherm, pore size distribution, DRIFTS, NMR spectra, detailed derivation for the cylindrical transport model, and replicate fittings ([PDF](#))

■ AUTHOR INFORMATION

Corresponding Authors

Omar K. Farha – Department of Chemistry and International Institute for Nanotechnology, Northwestern University, Evanston, Illinois 60208, United States; Department of Chemical and Biological Engineering, Northwestern University, Evanston, Illinois 60208, United States;
[ORCID.org/0000-0002-9904-9845](#); Email: o-farha@northwestern.edu

Randall Q. Snurr – Department of Chemical and Biological Engineering, Northwestern University, Evanston, Illinois 60208, United States; [ORCID.org/0000-0003-2925-9246](#); Email: snurr@northwestern.edu

Kaihang Shi – Department of Chemical and Biological Engineering, Northwestern University, Evanston, Illinois 60208, United States; Department of Chemical and Biological Engineering, University at Buffalo, The State University of New York, Buffalo, New York 14260, United States; [ORCID.org/0000-0002-0297-1746](#); Email: kaihangs@buffalo.edu

Author

Florencia A. Son – Department of Chemistry and International Institute for Nanotechnology, Northwestern University, Evanston, Illinois 60208, United States;
[ORCID.org/0000-0002-7524-3774](#)

Complete contact information is available at: <https://pubs.acs.org/10.1021/acsami.4c02117>

Author Contributions

F.A.S. and K.S. contributed equally to this work.

Notes

The authors declare the following competing financial interest(s): O.K.F. and R.Q.S. have a financial interest in NuMat Technologies, a startup company that is seeking to commercialize MOFs.

■ ACKNOWLEDGMENTS

O.K.F. and R.Q.S. gratefully acknowledge support from the Defense Threat Reduction Agency (HDTRA1-19-1-0007). K.S. gratefully acknowledges the startup funds from the University at Buffalo. This work made use of the IMSERC X-ray facility at Northwestern University, which has received

support from the Soft and Hybrid Nanotechnology Experimental (SHyNE) Resource (NSF ECCS-2025633), and Northwestern University. This work also made use of the EPIC facility of Northwestern University's NU Center, which has received support from the SHyNE Resource (NSF ECCS-2025633), the IIN, and Northwestern's MRSEC program (NSF DMR-1720139). F.A.S. is supported by the Department of Defense (DoD) through the National Defense Science & Engineering Graduate (NDSEG) Fellowship Program and the Ryan Fellowship through the International Institute for Nanotechnology at Northwestern University. F.A.S. also thanks Shengyi (Tony) Su and Dr. Saptasree Bose for helpful discussions.

■ REFERENCES

- (1) Furukawa, H.; Cordova, K. E.; O'Keeffe, M.; Yaghi, O. M. The Chemistry and Applications of Metal-Organic Frameworks. *Science* **2013**, *341*, 1230444.
- (2) Wang, J.; Zhang, Y.; Su, Y.; Liu, X.; Zhang, P.; Lin, R. B.; Chen, S.; Deng, Q.; Zeng, Z.; Deng, S.; Chen, B. Fine Pore Engineering in a Series of Isoreticular Metal-Organic Frameworks for Efficient C2H2/CO2 Separation. *Nat. Commun.* **2022**, *13*, 200.
- (3) Syed, Z. H.; Mian, M. R.; Patel, R.; Xie, H.; Pengmei, Z.; Chen, Z.; Son, F. A.; Goetjen, T. A.; Chapovetsky, A.; Fahy, K. M.; et al. Sulfated Zirconium Metal-Organic Frameworks as Well-Defined Supports for Enhancing Organometallic Catalysis. *J. Am. Chem. Soc.* **2022**, *144*, 16883–16897.
- (4) Wang, S.; Lee, J. S.; Wahiduzzaman, M.; Park, J.; Muschi, M.; Martineau-Corcos, C.; Tissot, A.; Cho, K. H.; Marrot, J.; Shepard, W.; Maurin, G.; Chang, J. S.; Serre, C. A Robust Large-Pore Zirconium Carboxylate Metal-Organic Framework for Energy-Efficient Water-Sorption-Driven Refrigeration. *Nat. Energy* **2018**, *3* (11), 985–993.
- (5) Kim, E. J.; Siegelman, R. L.; Jiang, H. Z. H.; Forse, A. C.; Lee, J. H.; Martell, J. D.; Milner, P. J.; Falkowski, J. M.; Neaton, J. B.; Reimer, J. A.; Weston, S. C.; Long, J. R. Cooperative Carbon Capture and Steam Regeneration with Tetraamine-Appended Metal-Organic Frameworks. *Science* (1979) **2020**, *369* (6502), 392–396.
- (6) Mondloch, J. E.; Katz, M. J.; Isley, W. C., III; Ghosh, P.; Liao, P.; Bury, W.; Wagner, G. W.; Hall, M. G.; DeCoste, J. B.; Peterson, G. W.; Snurr, R. Q.; Cramer, C. J.; Hupp, J. T.; Farha, O. K. Destruction of Chemical Warfare Agents Using Metal-Organic Frameworks. *Nat. Mater.* **2015**, *14*, 512–516.
- (7) Valizadeh, B.; Nguyen, T. N.; Stylianou, K. C. Shape Engineering of Metal-Organic Frameworks. *Polyhedron* **2018**, *145*, 1–15.
- (8) Perego, C.; Villa, P. Catalyst Preparation Methods. *Catal. Today* **1997**, *34*, 281–305.
- (9) Ren, J.; Langmi, H. W.; North, B. C.; Mathe, M. Review on Processing of Metal-Organic Framework (MOF) Materials towards System Integration for Hydrogen Storage. *Int. J. Energy Res.* **2015**, *39*, 607–620.
- (10) Riva, L.; Nielsen, H. K.; Skreiberg, Ø.; Wang, L.; Bartocci, P.; Barbanera, M.; Bidini, G.; Fantozzi, F. Analysis of Optimal Temperature, Pressure and Binder Quantity for the Production of Biocarbon Pellet to Be Used as a Substitute for Coke. *Appl. Energy* **2019**, *256*, 113933.
- (11) Peterson, G. W.; Decoste, J. B.; Glover, T. G.; Huang, Y.; Jasuja, H.; Walton, K. S. Effects of Pelletization Pressure on the Physical and Chemical Properties of the Metal-Organic Frameworks Cu3(BTC)₂ and UiO-66. *Microporous Mesoporous Mater.* **2013**, *179*, 48–53.
- (12) Zhang, Y.; Feng, X.; Li, H.; Chen, Y.; Zhao, J.; Wang, S.; Wang, L.; Wang, B. Photoinduced Postsynthetic Polymerization of a Metal-Organic Framework toward a Flexible Stand-Alone Membrane. *Angew. Chem., Int. Ed.* **2015**, *54* (14), 4259–4263.
- (13) Aguado, S.; Canivet, J.; Farrusseng, D. Facile Shaping of an Imidazolate-Based MOF on Ceramic Beads for Adsorption and Catalytic Applications. *Chem. Commun.* **2010**, *46* (42), 7999–8001.

- (14) Pinto, M. L.; Dias, S.; Pires, J. Composite MOF Foams: The Example of UiO-66/Polyurethane. *ACS Appl. Mater. Interfaces* **2013**, *5* (7), 2360–2363.
- (15) Ma, K.; Idrees, K. B.; Son, F. A.; Maldonado, R.; Wasson, M. C.; Zhang, X.; Wang, X.; Shehayeb, E.; Merhi, A.; Kaafarani, B. R.; Islamoglu, T.; Xin, J. H.; Farha, O. K. Fiber Composites of Metal-Organic Frameworks. *Chem. Mater.* **2020**, *32* (17), 7120–7140.
- (16) Kitao, T.; Zhang, Y.; Kitagawa, S.; Wang, B.; Uemura, T. Hybridization of MOFs and Polymers. *Chem. Soc. Rev.* **2017**, *46* (11), 3108–3133.
- (17) Kalaj, M.; Denny, M. S.; Bentz, K. C.; Palomba, J. M.; Cohen, S. M. Nylon-MOF Composites through Postsynthetic Polymerization. *Angewandte Chemie - International Edition* **2019**, *58* (8), 2336–2340.
- (18) Ma, K.; Wang, Y.; Chen, Z.; Islamoglu, T.; Lai, C.; Wang, X.; Fei, B.; Farha, O. K.; Xin, J. H. Facile and Scalable Coating of Metal-Organic Frameworks on Fibrous Substrates by a Coordination Replication Method at Room Temperature. *ACS Appl. Mater. Interfaces* **2019**, *11* (25), 22714–22721.
- (19) Chen, Z.; Ma, K.; Mahle, J. J.; Wang, H.; Syed, Z. H.; Atilgan, A.; Chen, Y.; Xin, J. H.; Islamoglu, T.; Peterson, G. W.; Farha, O. K. Integration of Metal-Organic Frameworks on Protective Layers for Destruction of Nerve Agents under Relevant Conditions. *J. Am. Chem. Soc.* **2019**, *141* (51), 20016–20021.
- (20) Ma, K.; Islamoglu, T.; Chen, Z.; Li, P.; Wasson, M. C.; Chen, Y.; Wang, Y.; Peterson, G. W.; Xin, J. H.; Farha, O. K. Scalable and Template-Free Aqueous Synthesis of Zirconium-Based Metal-Organic Framework Coating on Textile Fiber. *J. Am. Chem. Soc.* **2019**, *141* (39), 15626–15633.
- (21) Dwyer, D. B.; Dugan, N.; Hoffman, N.; Cooke, D. J.; Hall, M. G.; Tovar, T. M.; Bernier, W. E.; Decoste, J.; Pomerantz, N. L.; Jones, W. E. Chemical Protective Textiles of UiO-66-Integrated PVDF Composite Fibers with Rapid Heterogeneous Decontamination of Toxic Organophosphates. *ACS Appl. Mater. Interfaces* **2018**, *10* (40), 34585–34591.
- (22) McCarthy, D. L.; Liu, J.; Dwyer, D. B.; Troiano, J. L.; Boyer, S. M.; Decoste, J. B.; Bernier, W. E.; Jones, W. E., Jr. Electrospun Metal-Organic Framework Polymer Composites for the Catalytic Degradation of Methyl Paraoxon. *New J. Chem.* **2017**, *41* (17), 8748–8753.
- (23) da Silva Pinto, M.; Sierra-Avila, C. A.; Hinestroza, J. P. In Situ Synthesis of a Cu-BTC Metal-Organic Framework (MOF 199) onto Cellulosic Fibrous Substrates: Cotton. *Cellulose* **2012**, *19* (5), 1771–1779.
- (24) Chen, Y.; Li, S.; Pei, X.; Zhou, J.; Feng, X.; Zhang, S.; Cheng, Y.; Li, H.; Han, R.; Wang, B. A Solvent-Free Hot-Pressing Method for Preparing Metal-Organic-Framework Coatings. *Angew. Chem., Int. Ed.* **2016**, *55* (10), 3419–3423.
- (25) Peterson, G. W.; Lee, D. T.; Barton, H. F.; Epps, T. H.; Parsons, G. N. Fibre-Based Composites from the Integration of Metal-Organic Frameworks and Polymers. *Nat. Rev. Mater.* **2021**, *6* (7), 605–621.
- (26) Zhao, J.; Lee, D. T.; Yaga, R. W.; Hall, M. G.; Barton, H. F.; Woodward, I. R.; Oldham, C. J.; Walls, H. J.; Peterson, G. W.; Parsons, G. N. Ultra-Fast Degradation of Chemical Warfare Agents Using MOF-Nanofiber Kebabs. *Angew. Chem., Int. Ed.* **2016**, *55* (42), 13224–13228.
- (27) Lee, D. T.; Zhao, J.; Peterson, G. W.; Parsons, G. N. Catalytic “MOF-Cloth” Formed via Directed Supramolecular Assembly of UiO-66-NH₂ Crystals on Atomic Layer Deposition-Coated Textiles for Rapid Degradation of Chemical Warfare Agent Simulants. *Chem. Mater.* **2017**, *29* (11), 4894–4903.
- (28) Lu, A. X.; McEntee, M.; Browne, M. A.; Hall, M. G.; Decoste, J. B.; Peterson, G. W. MOFabric: Electrospun Nanofiber Mats from PVDF/UiO-66-NH₂ for Chemical Protection and Decontamination. *ACS Appl. Mater. Interfaces* **2017**, *9* (15), 13632–13636.
- (29) López-Maya, E.; Montoro, C.; Rodríguez-Albelo, L. M.; Aznar Cervantes, S. D.; Lozano-Pérez, A. A.; Cenís, J. L.; Barea, E.; Navarro, J. A. R. Textile/Metal-Organic-Framework Composites as Self-Detoxifying Filters for Chemical-Warfare Agents. *Angew. Chem., Int. Ed.* **2015**, *54* (23), 6790–6794.
- (30) Lee, D. T.; Jamir, J. D.; Peterson, G. W.; Parsons, G. N. Protective Fabrics: Metal-Organic Framework Textiles for Rapid Photocatalytic Sulfur Mustard Simulant Detoxification. *Matter* **2020**, *2* (2), 404–415.
- (31) Karger, J.; Ruthven, D. M.; Theodorou, D. N. *Diffusion in Nanoporous Materials*; Wiley-VCH Verlag & Co. KGaA: Weinheim, Germany, 2012.
- (32) Kärger, J.; Ruthven, D. M. Diffusion in Nanoporous Materials: Fundamental Principles, Insights and Challenges. *New J. Chem.* **2016**, *40* (5), 4027–4048.
- (33) Gao, W.; Cardenal, A. D.; Wang, C.; Powers, D. C. In Operando Analysis of Diffusion in Porous Metal-Organic Framework Catalysts. *Chem.—Eur. J.* **2019**, *25* (14), 3465–3476.
- (34) Teesdale, J. J.; Lee, M.; Lu, R.; Smith, Z. P. Uncertainty in Composite Membranes: From Defect Engineering to Film Processing. *J. Am. Chem. Soc.* **2023**, *145* (2), 830–840.
- (35) García-Salaberri, P. A.; Hwang, G.; Vera, M.; Weber, A. Z.; Gostick, J. T. Effective Diffusivity in Partially-Saturated Carbon-Fiber Gas Diffusion Layers: Effect of through-Plane Saturation Distribution. *Int. J. Heat Mass Transf.* **2015**, *86*, 319–333.
- (36) Alsyouri, H. M.; Lin, J. Y. S. Gas Diffusion and Microstructural Properties of Ordered Mesoporous Silica Fibers. *J. Phys. Chem. B* **2005**, *109* (28), 13623–13629.
- (37) McIntyre, S. R.; Hunter-Sellars, E.; Saenz-Cavazos, P. A.; Houghton, A. R.; Williams, D. R. Novel Zero-Length Column Analysis of Desorption Curves for Single Cylindrical Pellets. *Powder Technol.* **2023**, *416*, 118207.
- (38) Céline, A.; Fréour, S.; Jacquemin, F.; Casari, P. Characterization and Modeling of the Moisture Diffusion Behavior of Natural Fibers. *J. Appl. Polym. Sci.* **2013**, *130* (1), 297–306.
- (39) Arnold, J. C.; Alston, S. M.; Korkees, F. An Assessment of Methods to Determine the Directional Moisture Diffusion Coefficients of Composite Materials. *Compos Part A Appl. Sci. Manuf.* **2013**, *55*, 120–128.
- (40) Wang, R.; Shi, K.; Liu, J.; Snurr, R. Q.; Hupp, J. T. Water-Accelerated Transport: Vapor-Phase Nerve Agent Simulant Delivery within a Catalytic Zirconium Metal-Organic Framework as a Function of Relative Humidity. *J. Am. Chem. Soc.* **2023**, *145* (25), 13979–13988.
- (41) Titze, T.; Lauerer, A.; Heinke, L.; Chmelik, C.; Zimmermann, N. E. R.; Keil, F. J.; Ruthven, D. M.; Kärger, J. Transport in Nanoporous Materials Including MOFs: The Applicability of Fick’s Laws. *Angew. Chem., Int. Ed.* **2015**, *54* (48), 14580–14583.
- (42) Furukawa, H.; Gandara, F.; Zhang, Y.-B.; Jiang, J.; Queen, W. L.; Hudson, M. R.; Yaghi, O. M. Water Adsorption in Porous Metal-Organic Frameworks and Related Materials. *J. Am. Chem. Soc.* **2014**, *136* (11), 4369–4381.
- (43) Liu, X.; Kirlikovali, K. O.; Chen, Z.; Ma, K.; Idrees, K. B.; Cao, R.; Zhang, X.; Islamoglu, T.; Liu, Y.; Farha, O. K. Small Molecules, Big Effects: Tuning Adsorption and Catalytic Properties of Metal-Organic Frameworks. *Chem. Mater.* **2021**, *33*, 1444–1454.
- (44) Patel, H. A.; Yavuz, C. T. Noninvasive Functionalization of Polymers of Intrinsic Microporosity for Enhanced CO₂ Capture. *Chem. Commun.* **2012**, *48* (80), 9989–9991.
- (45) Jung, D.; Das, P.; Atilgan, A.; Li, P.; Hupp, J. T.; Islamoglu, T.; Kalow, J. A.; Farha, O. K. Reactive Porous Polymers for Detoxification of a Chemical Warfare Agent Simulant. *Chem. Mater.* **2020**, *32* (21), 9299–9306.
- (46) Jung, D.; Su, S.; Syed, Z. H.; Atilgan, A.; Wang, X.; Sha, F.; Lei, Y.; Gianneschi, N. C.; Islamoglu, T.; Farha, O. K. A Catalytically Accessible Polyoxometalate in a Porous Fiber for Degradation of a Mustard Gas Simulant. *ACS Appl. Mater. Interfaces* **2022**, *14* (14), 16687–16693.
- (47) Budd, P. M.; Elabas, E. S.; Ghanem, B. S.; Makhseed, S.; McKeown, N. B.; Msayib, K. J.; Tattershall, C. E.; Wang, D. Solution-Processed, Organophilic Membrane Derived from a Polymer of Intrinsic Microporosity. *Adv. Mater.* **2004**, *16* (5), 456–459.
- (48) McKeown, N. B.; Budd, P. M.; Msayib, K. J.; Ghanem, B. S.; Kingston, H. J.; Tattershall, C. E.; Makhseed, S.; Reynolds, K. J.;

- Fritsch, D. Polymers of Intrinsic Microporosity (PIMs): Bridging the Void between Microporous and Polymeric Materials. *Chem.—Eur. J.* **2005**, *11* (9), 2610–2620.
- (49) Budd, P. M.; Makhseed, S. M.; Ghanem, B. S.; Msayib, K. J.; Tattershall, C. E.; McKeown, N. B. Microporous Polymeric Materials. *Mater. Today* **2004**, *7* (4), 40–46.
- (50) Jung, D.; Kirlikovali, K. O.; Chen, Z.; Idrees, K. B.; Atilgan, A.; Cao, R.; Islamoglu, T.; Farha, O. K. An Amidoxime-Functionalized Porous Reactive Fiber against Toxic Chemicals. *ACS Mater. Lett.* **2021**, *3* (4), 320–326.
- (51) Lasseguette, E.; Malpass-Evans, R.; Casalini, S.; McKeown, N. B.; Ferrari, M. C. Optimization of the Fabrication of Amidoxime Modified PIM-1 Electrospun Fibres for Use as Breathable and Reactive Materials. *Polymer (Guildf)* **2021**, *213*, 123205.
- (52) Son, F. A.; Bukowski, B. C.; Islamoglu, T.; Snurr, R. Q.; Farha, O. K. Rapid Quantification of Mass Transfer Barriers in Metal-Organic Framework Crystals. *Chem. Mater.* **2021**, *33*, 9093–9100.
- (53) Brandani, S. Analysis of the Piezometric Method for the Study of Diffusion in Microporous Solids: Isothermal Case. *Adsorption* **1998**, *4*, 17–24.
- (54) Topuz, F.; Satilmis, B.; Uyar, T. Electrospinning of Uniform Nanofibers of Polymers of Intrinsic Microporosity (PIM-1): The Influence of Solution Conductivity and Relative Humidity. *Polymer (Guildf)* **2019**, *178*, 121610.
- (55) Brandani, S.; Brandani, F.; Mangano, E.; Pullumbi, P. Using a Volumetric Apparatus to Identify and Measure the Mass Transfer Resistance in Commercial Adsorbents. *Microporous Mesoporous Mater.* **2020**, *304*, 109277.
- (56) Brandani, S.; Mangano, E.; Brandani, F.; Pullumbi, P. Carbon Dioxide Mass Transport in Commercial Carbon Molecular Sieves Using a Volumetric Apparatus. *Sep Purif Technol.* **2020**, *245*, 116862.
- (57) Crank, J. *The Mathematics of Diffusion*, 2nd ed.; Oxford University Press Inc.: New York, 1975.
- (58) Heinke, L.; Kärger, J. Assessing One-Dimensional Diffusion in Nanoporous Materials from Transient Concentration Profiles. *New J. Phys.* **2008**, *10* (2), 023035.
- (59) Kärger, J. Transport Phenomena in Nanoporous Materials. *ChemPhysChem* **2015**, *16* (1), 24–51.
- (60) Hibbe, F.; Chmelik, C.; Heinke, L.; Pramanik, S.; Li, J.; Ruthven, D. M.; Tzoulaki, D.; Kärger, J. The Nature of Surface Barriers on Nanoporous Solids Explored by Microimaging of Transient Guest Distributions. *J. Am. Chem. Soc.* **2011**, *133* (9), 2804–2807.
- (61) Karwacki, L.; Kox, M. H. F.; Matthijs De Winter, D. A.; Drury, M. R.; Meeldijk, J. D.; Stavitski, E.; Schmidt, W.; Mertens, M.; Cubillas, P.; John, N.; Chan, A.; Kahn, N.; Bare, S. R.; Anderson, M.; Kornatowski, J.; Weckhuysen, B. M. Morphology-Dependent Zeolite Intergrowth Structures Leading to Distinct Internal and Outer-Surface Molecular Diffusion Barriers. *Nat. Mater.* **2009**, *8*, 959–965.
- (62) Bukowski, B. C.; Son, F. A.; Chen, Y.; Robison, L.; Islamoglu, T.; Snurr, R. Q.; Farha, O. K. Insights into Mass Transfer Barriers in Metal-Organic Frameworks. *Chem. Mater.* **2022**, *34*, 4134–4141.
- (63) Chen, Y.; Zhang, X.; Mian, M. R.; Son, F. A.; Zhang, K.; Cao, R.; Chen, Z.; Lee, S. J.; Idrees, K. B.; Goetjen, T. A.; et al. Structural Diversity of Zirconium Metal-Organic Frameworks and Effect on Adsorption of Toxic Chemicals. *J. Am. Chem. Soc.* **2020**, *142* (51), 21428–21438.
- (64) Son, F. A.; Wasson, M. C.; Islamoglu, T.; Chen, Z.; Gong, X.; Hanna, S. L.; Lyu, J.; Wang, X.; Idrees, K. B.; Mahle, J. J.; et al. Uncovering the Role of Metal-Organic Framework Topology on the Capture and Reactivity of Chemical Warfare Agents. *Chem. Mater.* **2020**, *32*, 4609–4617.
- (65) Agrawal, M.; Boulfelfel, S. E.; Sava Gallis, D. F.; Greathouse, J. A.; Sholl, D. S. Determining Diffusion Coefficients of Chemical Warfare Agents in Metal-Organic Frameworks. *J. Phys. Chem. Lett.* **2019**, *10* (24), 7823–7830.
- (66) Bukowski, B. C.; Snurr, R. Q. Insights and Heuristics for Predicting Diffusion Rates of Chemical Warfare Agents in Zirconium Metal-Organic Frameworks. *ACS Appl. Mater. Interfaces* **2022**, *14* (50), 55608–55615.
- (67) Emelianova, A.; Basharova, E. A.; Kolesnikov, A. L.; Arribas, E. V.; Ivanova, E. V.; Gor, G. Y. Force Fields for Molecular Modeling of Sarin and Its Simulants: DMMP and DIMP. *J. Phys. Chem. B* **2021**, *125* (16), 4086–4098.